scientific reports



OPEN

Fractional differential quadrature method for modeling composite halide perovskite solar cells

Ehab M. Almetwally^{1⊠}, Ola Ragb², Mohamed Salah² & Mokhtar Mohamed^{3⊠}

This work presents a novel approach for high-efficiency modeling of composite halide perovskite solar cells using the Fractional Differential Quadrature (FDQ) method. The FDQ method is applied to solve the governing equations derived from continuity and Poisson equations describing charge transport in a specific perovskite structure (PCBM/CH3NH3Gel3/Cul) solar cell. Our simulations demonstrate high accuracy with an error margin of 10⁻⁸ compared to experimental data and significant computational efficiency compared to other experimental and numerical methods. A detailed parametric study investigated the influence of temperature, layer thickness, charge carrier mobilities, and bandgaps on key performance indicators, including short-circuit current (Jsc), open-circuit voltage (Voc), fill factor (FF), and power conversion efficiency (PCE). Key findings include a maximum Jsc with a 300 nm increase in HTL thickness, a 7.5% decrease in PCE with a 50 nm increase in ETL thickness. These results provide valuable insights for optimizing the design and fabrication of high-performance composite halide perovskite solar cells and demonstrate the potential of the FDQ method as a powerful tool for device modeling and optimization.

Keywords Fractional differential quadrature, Caputo method, Discrete singular convolution, Block marching method, Composites cells, Halide perovskite solar cells

The literature surrounding perovskite solar cell technology has evolved significantly over the past several years, reflecting advancements in efficiency, stability, and material composition. In the foundational work by the authors emphasize the exceptional properties of perovskite solar cells compared to traditional thin-film technologies, particularly through interface engineering. They highlight the importance of optimizing interfacial work functions and charge transport capabilities, while also addressing challenges such as film morphology and lead toxicity, which continue to hinder large-scale applications. Building upon these insights², provide an integrated lifecycle assessment that underscores the remarkable efficiency of single-junction devices reaching 27%. Their review situates perovskite technology within the broader landscape of photovoltaic advancements, reinforcing the notion that perovskite solar cells are not only cost-effective but also capable of achieving high efficiencies comparable to silicon-based alternatives. This work is pivotal in establishing a more accurate representation of the current state of perovskite technology. Tang et al.³ further contribute to the discourse by documenting the rapid rise in efficiency of perovskite-based solar cells, from a mere 3.8% in 2009 to 22.1% in 2016. Their analysis highlights the environmental friendliness and low-cost potential of halide perovskites, while also addressing the critical issue of stability, which remains a barrier to commercialization.

In the following year, Shen et al.⁴ discuss the evolution of tandem designs in perovskite photovoltaics, noting certified efficiencies for single-junction cells reaching 23%. Their findings illustrate the significant progress made in integrating perovskite materials with silicon, demonstrating the potential for enhanced performance through tandem configurations. Dharmadasa et al.⁵ provide a deep analysis of the efficiency metrics of perovskite solar cells, documenting experimental efficiencies between 14–15%. They emphasize the unique physical properties of perovskite materials, which have led to substantial improvements in device performance over a short period. Nevertheless, they also caution about the ongoing challenges related to stability and toxicity. Shi et al.⁶ identify hybrid organic-inorganic perovskite solar cells as a burgeoning area of research, highlighting their advantages in light absorption and carrier diffusion. Their review critically examines the barriers to commercialization, including stability and lead toxicity, and proposes future research directions to address these challenges.

¹Department of Mathematics and Statistics, Faculty of Science, Imam Mohammad Ibn Saud Islamic University, (IMSIU), 11432 Riyadh, Saudi Arabia. ²Department of Engineering Mathematics and Physics, Faculty of Engineering, Zagazig University, P.O. 44519, Zagazig, Egypt. ³Department of Basic science, Faculty of Engineering, Delta University for Science and Technology, Gamasa, Egypt. [™]email: emalmetwally@imamu.edu.sa; Mokhtar.Alsaidi@deltauniv.edu.eg

The work of Trivedi et al.⁷ introduces advancements in the growth of high-quality single-crystal perovskite films, which are pivotal for achieving photovoltaic parameters close to theoretical limits. They emphasize the need for novel growth techniques and interface engineering to further enhance efficiency, which has already surpassed 21% for single-crystal devices. Siegrist et al.⁸ reiterate the significance of the recent achievement of 27% efficiency in single-junction devices, reinforcing the narrative of continuous improvement in perovskite technology. Their work highlights the necessity for updated methodologies and materials to maintain this upward trajectory. Chiang et al.⁹ delve into the optimization of dual-interface designs in all-perovskite tandem solar cells, showcasing the potential for multi-junction configurations to exceed the efficiency limits of single-junction cells. They advocate for innovative deposition methods to facilitate scalability and modularity in production. Finally, Yekra et al.¹⁰ explore the promising domain of lead-free mixed halide double perovskites, presenting a novel approach to enhancing the structural stability and efficiency of solar cells. Their findings indicate that CsTiIBr demonstrates significant potential, with reported efficiencies of 13.31%, paving the way for sustainable solar energy solutions.

Stoumpos et al. ¹¹ are the first using halide perovskite $CH_3NH_3GeI_3$ and noticing its structure composed of strong nonlinear optical features and greatly distorted construction. Krishnamoorthy et al. ¹² used the perovskite materials of lead-free Ge iodide and illustrated a strong potential in the applications of photovoltaic. Many studies described that the doping metal (Ge) mixed with (Pb) gives higher efficiency $(26\%)^{13-16}$. Due to the instability and toxicity of lead halide perovskites ^{17,18}, germanium (Ge) is being explored as a substitute for lead and tin in perovskite solar cells, as it shares the same subgroup ^{19,20}. The transport layers of solar cell are capable of decreasing the recombination of carriers at the boundary surfaces, which make the solar cell stability and efficiency increase. Several transport layers play a vital role in enhancing the solar cells performance. Hole transport layers (HTL) and electron transport layers (ETL) are the furthermost significant layers ²¹⁻²³. In this research, CH₃NH₃Gel₃ are used as a faultless light absorber in perovskite solar cells inserted between PCBM as ETL and CuI as HTL.

Experimentally, the performance of a halide perovskite solar cell inserted between two transport layers of electron and hole is analyzed recently by several researches, the influence of hole transport layer on halide perovskite solar cell mechanism was investigated by Kanoun et al.²⁴. Hossain et al.²⁵ produced an efficiency about 24% using CH3NH3PbI3 based solar cells with different HTL including Spiro-OMETAD, NiO, CuI, CuSCN, and Cu2O by wxAMPS and SCAPS software. Subbiah et al.²⁶ studied the inorganic HTL for perovskite solar cell experimentally. Kirchartz et al.²⁷ introduced experimental results with respect to recombination and open-circuit voltages in lead-halide perovskites. Belayachi et al.²⁸ experimentally studied the partial substitution of lead iodide (PbI₂) with the inorganic compound copper iodide (CuI) to enhance the solar cell stability. Wang et al.²⁹ used SnO₂ electron transport layer in perovskite solar cell and managed the band structure defects by using cobalt chloride hexahydrate (CoCl₂·6H₂O). They achieved an efficiency of 23.82% at gap energy of 1.54eV. Elseman al³⁰. produced an experimental study for analysis the impact of various halides on planar perovskite solar cell performance. Bajorowiczet al.³¹ produced experimental study to provide an insight into improving lead-free inorganic halide perovskite with stimulating optical and photo catalytic features. Haider et al.³² illustrated an analytical analysis for effecting thickness of HTL on perovskite solar cell and realized 21.06% efficiency.

Numerically, the performance of a halide PSCs inserted between two layers (HTL-ETL) is analyzed recently by several researches. Burgelman et al.³³ presented a simulation of halide perovskite solar cell using 1D-Solar Cell Capacitance Simulator software (SCAPS). Finite difference method is employed to study the properties of solar cell current and voltage by Van Reenen et al.³⁴. Ravishankar et al.³⁵ applied method of least-squares for investigating the model of surface polarization of perovskite solar cell. As well as, they offered detailed analysis for PSCs at both states (steady/transient). Two numerical techniques (finite element/difference) were applied to solve motion of ion vacancy in PSC model by Courtier et al.³⁶. Also, they showed that finite element scheme is best for calculating the efficiency. Finite element technique is applied to explain the modified structure of perovskite solar cell which leads to efficiency of 17.5%. Ragb et al.^{37,38} applied differential quadrature (DQ) method with several shape functions and achieved accurate results using less grid points. Also, they achieved efficiency about 32% for perovskite solar cell.

In this research, Fractional Differential Quadrature (FDQ) method is employed by using discrete singular convolution shape function with two kernels to analyze the composite halide PSC (PCBM/CH3NH3GeI3/CuI) performance. This scheme is introduced for the halide PSC to achieve higher efficiency. Then, we convert them to nonlinear algebraic system by using FDQ and block marching methods³⁹. Also, we apply the iterative technique to overcome nonlinearity problem^{37,40,41}. With the aid of the MATLAB program, we obtain an efficient and accurate results compared with preceding experiment and numerical studies. Subsequently, we introduce a parametric study including the effects of temperature, thickness of various layers, mobilities, and energy gaps on power conversion efficiency, open circuit voltage, fill factor, and current density of composite halide PSC.

The problem formulation

The model contains of halide perovskite CH3NH3GeI3 as absorber layer inserted between two layers. These layers are electron transport layer (ETL- PCBM) and hole transport layer (HTL-CuI)^{32,34-36,42-45} as illustrated in Fig. 1.

The halide perovskite layer (0 < z < L)

Based on drift and diffusion formulations, the governing equations at this layer can described as^{32,34,43}:

$$\frac{\partial^{\alpha} H}{\partial t^{\alpha}} + \frac{1}{e} \frac{\partial^{\beta} J_{H}}{\partial z^{\beta}} = G(z) - R(E, H), \tag{1}$$

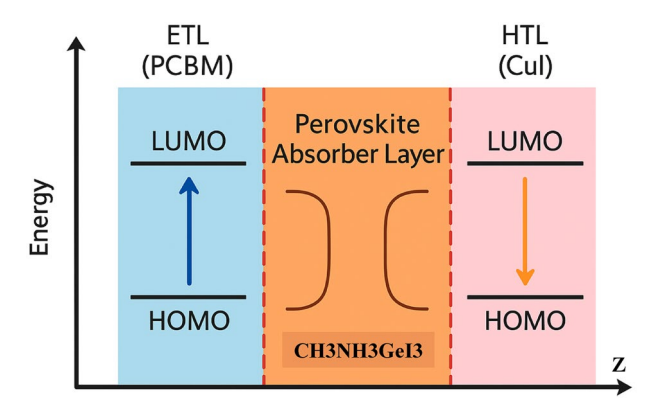


Fig. 1. Schematic of halide perovskite layer inserted between (ETL-PCBM) and (HTL-CuI).

$$\frac{\partial^{\alpha} E}{\partial t^{\alpha}} - \frac{1}{e} \frac{\partial^{\beta} J_{E}}{\partial z^{\beta}} = G(z) - R(E, H), \tag{2}$$

$$\frac{\partial^{\alpha} I}{\partial t^{\alpha}} + \frac{\partial^{\beta} F_I}{\partial z^{\beta}} = 0, \tag{3}$$

where "t" is the time and e" is the electric charge (e > 0). $\alpha \in]0,1[$ and $\beta \in]1,2[$ are the fractional order derivative. J_H, J_E sign to the holes and electrons currents densities respectively:

$$J_{H} = -eD_{H_{halide}} \left(\frac{\partial H}{\partial z} + \frac{H}{V_{T}} \frac{\partial \phi}{\partial z} \right), \tag{4}$$

$$J_E = eD_{E_{halide}} \left(\frac{\partial E}{\partial z} - \frac{E}{V_T} \frac{\partial \phi}{\partial z} \right), \tag{5}$$

 F_{τ} is the iodide ion flux which equals:

$$F_{I} = -\left(\frac{\partial H}{\partial z} + \frac{I}{V_{T}}\frac{\partial \phi}{\partial z}\right) / D_{I},\tag{6}$$

 ${
m V_T}$ is the thermal voltage. The ion vacancy, electron, and hole diffusion coefficients of halide perovskite material are denoted by D_I , $D_{E_{halide}}$, and $D_{H_{halide}}$, respectively. Using Poisson equation, the electrostatic potential ϕ can be calculated by as follow^{2,17–22,27}:

$$\frac{\partial^2 \phi}{\partial z^2} = \frac{e}{\varepsilon_p} (N_0 - I + N_E - N_H) \tag{7}$$

 N_0 signs to density of ion vacancies, $N_{\rm F}$ is electron dopant concentration, $N_{\rm H}$ is hole dopant concentration and ε_p signs to halide perovskite permittivity.

G(z) sign to the rate of generation computed as follow³⁶:

$$G(z) = F_{ph} \alpha e^{-\alpha z} \tag{8}$$

 F_{vh} signs to incident photon flux. Also, α expresses the coefficient of absorption. R is the rate of recombination which can be computed as 36 :

$$R = \frac{E \times H}{\tau_H E + \tau_E H} \tag{9}$$

where τ_E , τ_H are electron, hole lifetimes. The measurement of electron and hole lifetimes in perovskite materials is crucial in perovskite research. Photoluminescence (PL) decays and transient absorption (TA) spectroscopy are key techniques for quantifying these lifetimes⁴⁶. PL methods analyze emitted light to understand carrier dynamics and defect contributions, with studies on triple-cation perovskites showing that low-repetition-rate techniques are needed to capture long PL decay times⁴⁷. TA spectroscopy observes changes in absorption to study transient electron and hole states and distinguish between recombination channels. Accurate lifetime determination requires considering all mechanisms, potentially using non-adiabatic molecular dynamics (NAMD) simulations to account for defect density and recombination. Addressing challenges in experimental techniques and discrepancies in radiative recombination coefficients is vital for advancing perovskite materials for solar cells and optoelectronics.

Defect density is a crucial factor affecting the optoelectronic properties and performance of perovskite materials in solar cells and LEDs. Halide ions, crystal structure, and processing conditions influence the defect landscape. Defects can trap charge carriers and reduce their mobility, while increasing the dielectric constant can mitigate defect impacts. Recent techniques like Laplace current deep level transient spectroscopy allow detailed defect state measurements. Molecular passivators can reduce defect densities and enhance device performance by minimizing non-radiative recombination. Managing defect density is essential for developing high-performance perovskite materials and their commercial adoption⁴⁸. When examining a grain size (L) of approximately 300 nm, the derived surface defect density approximates 10¹⁶ cm⁻³, aligning closely with experimental findings in the field. The critical insights collected from the analysis of defect densities in perovskite materials illuminate the necessity of controlling grain size to control defect densities, ultimately enhancing the performance of perovskite solar cells. This line of inquiry not only deepens our understanding of defect dynamics in perovskites but also informs future strategies for material optimization in photovoltaic applications.

At the boundary of this layer, we can write the conditions as follow^{32,34–36,42–45}:

$$at \ z = 0 \ \begin{cases} F_{I} = 0 \\ J_{H} = -eR_{l} \end{cases}, \ R_{l} = \frac{E|_{z=0^{-}} \times H|_{z=0^{+}}}{H|_{z=0^{+}} / \nu_{EE} + E|_{z=0^{-}} / \nu_{HE}} \end{cases}$$

$$at \ z = L \ \begin{cases} F_{I} = 0 \\ J_{E} = -eR_{r} \end{cases}, \ R_{r} = \frac{E|_{z=L^{-}} H|_{z=L^{+}}}{H|_{z=L^{+}} / \nu_{EH} + E|_{z=L^{-}} / \nu_{HH}}, \end{cases}$$

$$(10)$$

where R_1 and R_2 are the surface recombination rates. ν is the Electron/Hole recombination velocity at interfaces.

The electron transport layer ($-L_E < z < 0$)

According to Poisson and Conservation equations for the free electrons, the governing equations at this layer can be introduced as follow $^{32,34-36,42-45}$:

$$\frac{\partial^{\alpha} E}{\partial t^{\alpha}} - \frac{1}{e} \frac{\partial^{\beta} J_{E}}{\partial z^{\beta}} = 0, \tag{11}$$

$$J_E = eD_E \left(\frac{\partial E}{\partial z} - \frac{E}{V_T} \frac{\partial \phi}{\partial z} \right), \tag{12}$$

$$\frac{\partial^2 \phi}{\partial z^2} = \frac{e}{\varepsilon_E} (E - d_n),\tag{13}$$

where d_n is the effective doping density for electrons, D_E is the diffusion coefficient of electrons and ε_E expresses the permittivity of ETL.

At the boundary of this layer, we can write the conditions as follow^{36,49}:

$$at z = -L_E \Rightarrow \begin{bmatrix} \phi \\ E \end{bmatrix} = \begin{bmatrix} 0 \\ d_n \end{bmatrix},$$
 (14)

The hole transport layer ($L < z < L + L_H$)

According to Poisson and Conservation equations for the free holes, the governing equations at this layer can be introduced as follow^{32,34–36,42–45}:

$$\frac{\partial^{\alpha} H}{\partial t^{\alpha}} + \frac{1}{e} \frac{\partial^{\beta} J_{H}}{\partial z^{\beta}} = 0, \tag{15}$$

$$J_H = -eD_H \left(\frac{\partial H}{\partial z} + \frac{H}{V_T} \frac{\partial \phi}{\partial z} \right), \tag{16}$$

$$\frac{\partial^2 \phi}{\partial z^2} = \frac{e}{\varepsilon_H} (d_p - H),\tag{17}$$

where d_p is hole effective doping density and ε_H expresses the permittivity of HTL.

The boundary condition at this layer can be written as 36,49 :

$$at \ z = L + L_H \Rightarrow \begin{bmatrix} \phi \\ H \end{bmatrix} = \begin{bmatrix} V_a(t) - V_{built} \\ d_p \end{bmatrix},$$
 (18)

where the applied voltage is represented by V_a and the built-in voltage by V_{built} .

At the boundary of interfaces, the continuity conditions can be introduced as follow⁵⁰:

$$\phi|_{z=0^{-}} = \phi|_{z=0^{+}}, \ \varepsilon_{E} \frac{\partial \phi}{\partial z}\Big|_{z=0^{-}} = \varepsilon_{p} \frac{\partial \phi}{\partial z}\Big|_{z=0^{+}}, \ k_{E} E|_{z=0^{-}} = E|_{z=0^{+}},$$
 (19)

$$\phi|_{z=L^{-}} = \phi|_{z=L^{+}}, \varepsilon_{p} \frac{\partial \phi}{\partial z}\Big|_{z=L^{-}} = \varepsilon_{H} \frac{\partial \phi}{\partial z}\Big|_{z=L^{+}}, H|_{z=L^{-}} = k_{H} H|_{z=L^{+}},$$
(20)

where $k_E = \frac{g_c}{d_n} \exp\left(\frac{E_C - E_{fE}}{eV_T}\right)$, $k_H = \frac{g_V}{d_p} \exp\left(\frac{E_V - E_{fH}}{eV_T}\right)$. E_C and E_V are minimum conduction band and maximum valence band respectively. g_C expresses the band of conduction and g_V

expresses the band of valence. E_{fE} and E_{fH} express Fermi level for electron and hole. By putting $\frac{\partial E}{\partial t} = \frac{\partial H}{\partial t} = \frac{\partial I}{\partial t} = 0$ in Eqs. (1,2,3,11,15), we can obtain the initial values where the previous governing equations are at steady state.

Method of solution

Firstly, Discrete singular convolution differential quadrature (DQ) method combined with the technique of block-marching to analyze the halide perovskite CH3NH3GeI3 layer inserted between two layers (Electron transport layer- Hole transport layer) at $\alpha=1$ and $\beta=2^{32,34-36,42-45}$.

Discrete singular convolution differential quadrature method

We express the concept of singular convolution as $^{51-54}$

$$F(t) = (T \times \eta)(t) = \int_{-\infty}^{\infty} T(t-z) \, \eta(z) \, dz \tag{21}$$

where T(t-z) is a kernel of singular and $\eta(t)$ express the trial function space part.

The discrete singular convolution differential quadrature method is governed by type of kernel. So, we show it as follow:

(a) Delta lagrange kernel (DLK)

This research employed the undefined \Re with its corresponding $\Re^{(r)}$ as an approach where the function is represented by a weighted linear sum of nodal values, \Re_i , as described in 51–54.

$$\Re(z_i) = \sum_{j=-M}^{M} \frac{1}{(z_i - z_j)} \times \frac{\prod_{k=-M}^{M} (z_i - z_k)}{\prod_{j=-M, \ k \neq i, j}^{M} (z_j - z_k)} \times \Re(z_j), \qquad (i = -N \text{ to } N), \ M \ge 1$$
 (22)

$$\frac{\partial^r \Re}{\partial z^r} \Big|_{z=z_i} = \sum_{j=1}^N a_{ij}^{(r)} \Re(z_j), \quad \text{where } i = -N : N , \quad \Re(E, H, J_E, J_H, I, F_I)$$
 (23)

 $a_{ii}^{(1)}$ and $\mathbf{a}_{ii}^{(2)}$ can be determined as $^{51-54}$:

$$a_{ij}^{(1)} = \begin{cases} \frac{1}{(z_i - z_j)} \prod_{\substack{k = -M, \\ k \neq i, j}}^{M} \frac{(z_i - z_k)}{(z_j - z_k)} & i \neq j \\ -\sum_{\substack{j = -M, \\ j \neq i}}^{M} a_{ij}^{(1)} & i = j \end{cases}, \quad a_{ij}^{(2)} = \begin{cases} 2\left(a_{ij}^{(1)} a_{ii}^{(1)} - \frac{a_{ij}^{(1)}}{(z_i - z_j)}\right) & i \neq j \\ -\sum_{\substack{j = -M, \\ j \neq i}}^{M} a_{ij}^{(2)} & i = j \end{cases}, \quad (24)$$

(b) Regularized shannon kernel (RSK):

Similarly, at this kernel, the unknown \Re with its corresponding $\Re^{(r)}$ is approximated by a weighted linear sum of nodal values, \Re_i , as described in^{51–54}.

$$\psi(z_i) = \sum_{j=-M}^{M} \left\langle \frac{\sin[\pi(z_i - z_j)/h_z]}{\pi(z_i - z_j)/h_z} \exp(\frac{-(z_i - z_j)^2}{2\sigma^2}) \right\rangle \psi(z_j), \quad (i = -N:N), \sigma = (\rho * h_z) > 0 \quad (25)$$

where σ and ρ are considered factors of regularization and computational respectively. $a_{ij}^{(1)}$ and $a_{ij}^{(2)}$ can be calculated as37:

$$a_{ij}^{(1)} = \begin{cases} \frac{(-1)^{i-j}}{h_z(i-j)} \exp(-h_z^2(\frac{(i-j)^2}{2\sigma^2})), & i \neq j \\ 0 & i = j \end{cases}, a_{ij}^{(2)} = \begin{cases} \frac{(2(-1)^{i-j+1}}{h_z^2(i-j)^2} + \frac{1}{\sigma^2}) \exp(-h_z^2(\frac{(i-j)^2}{2\sigma^2})), & i \neq j \\ -\frac{1}{\sigma^2} - \frac{\pi^2}{3h_z^2} & i = j \end{cases}$$
(26)

After this conversation, it's shown that selection the suitable kernel, bandwidth (2 M + 1) and grid points (N) play a dynamic role in obtaining the most accuracy results.

Block-marching technique

In order to solve the governing equations of the model at transient state, the block-marching technique is augmented with discrete singular convolution differential quadrature method. The time domain is distributed into some time intervals \triangle t_1 , \triangle t_2 , \triangle t_3 ,.... Every block includes one interval \triangle t at z-direction from 0 to L_x.

The weighting coefficients depend on the grid points coordinates. The distribution of mesh size is identical at all blocks. We employ these weighting coefficients at all blocks by equating $\Delta t_1 = \Delta t_2 = \Delta t_3$ In nth block, the next grid points are applied in z and t directions⁵⁵:

$$z_i = \frac{L_z}{2} \left(1 - \cos \left(\frac{i-1}{N-1} \pi \right) \right), \quad (i=1:N)$$
 (27)

$$t_k = (K - 1) \Delta t + \frac{\Delta t}{2} \left[1 - \cos\left(\frac{k - 1}{\ell - 1}\pi\right) \right], \quad (k = 1 : \ell)$$
 (28)

where K signs to the order of block, N is the grid point in z direction and ℓ signs to the block time level.

Using Block-Marching technique in Eqs. (21–26) into electron transport layer governing Eqs. (11–13) as follow:

For electron transport layer (ETL):

$$\sum_{j=1}^{L} \overline{a}_{ij}^{(1)} E_j - \frac{1}{e} \sum_{j=1}^{N} a_{ij}^{(1)} J_{E_j} = 0,$$
(29)

$$\sum_{j=1}^{N} \delta_{ij} J_{E_j} = e \times D_E \sum_{j=1}^{L} a_{ij}^{(1)} E_j - e \times D_E \frac{\sum_{k=1}^{N} \delta_{ik} E_k \times \sum_{j=1}^{N} a_{ij}^{(1)} \phi_j}{V_T},$$
(30)

$$\sum_{j=1}^{N} a_{ij}^{(2)} \phi_j - \frac{e}{\varepsilon_E} \sum_{j=1}^{N} \delta_{ij} E_j = -\frac{e}{\varepsilon_E} \times d_n, \tag{31}$$

where $\bar{a}_{ij}^{(1)}$ expresses the weighting coefficient of 1st derivative with respect to time.

Now, there is nonlinear algebraic system contains three Eqs. (29–31) with unknowns of (E, J_E , ϕ) resolved to cultivate the values of (E, J_E , ϕ) at ETL.

Additionally, applying the block-marching technique from Eqs. (21–26) to the governing equations of the hole transport layer (15–17) as follows:

For hole transport layer (HTL):

$$\sum_{j=1}^{L} \overline{a}_{ij}^{(1)} H_j + \frac{1}{e} \sum_{j=1}^{N} a_{ij}^{(1)} J_{H_j} = 0,$$
(32)

$$\sum_{j=1}^{N} \delta_{ij} J_{H_j} = -e \times D_H \sum_{j=1}^{L} a_{ij}^{(1)} H_j - e \times D_H \frac{\sum_{k=1}^{N} \delta_{ik} H_k \times \sum_{j=1}^{N} a_{ij}^{(1)} \phi_j}{V_T},$$
(33)

$$\sum_{j=1}^{N} a_{ij}^{(2)} \phi_j + \frac{e}{\varepsilon_H} \sum_{j=1}^{N} \delta_{ij} H_j = \frac{e}{\varepsilon_H} \times d_p, \tag{34}$$

Also, there is nonlinear algebraic system contains three Eqs. (32–34) with unknowns of (H, J_H , ϕ) resolved to cultivate the values of (H, J_H , ϕ) at HTL.

Consequently, the following is the application of block-marching from Eqs. (21–26) to interface Eqs. (19–20):

At the interfaces:

$$\sum_{j=1}^{N} \delta_{ij} \phi_{j} \bigg|_{z=0^{-}} = \sum_{j=1}^{N} \delta_{ij} \phi_{j} \bigg|_{z=0^{+}}, \quad \varepsilon_{E} \sum_{j=1}^{N} a_{ij}^{(1)} \phi_{j} \bigg|_{z=0^{-}} = \varepsilon_{p} \sum_{j=1}^{N} a_{ij}^{(1)} \phi_{j} \bigg|_{z=0^{+}}, \quad (35)$$

$$k_E \sum_{j=1}^{N} \delta_{ij} E_j \bigg|_{z=0^-} = \sum_{j=1}^{N} \delta_{ij} E_j \bigg|_{z=0^+}$$
(36)

$$\sum_{j=1}^{N} \delta_{ij} \phi_{j} \bigg|_{z=d^{-}} = \sum_{j=1}^{N} \delta_{ij} \phi_{j} \bigg|_{z=d^{+}}, \qquad \varepsilon_{p} \sum_{j=1}^{N} a_{ij}^{(1)} \phi_{j} \bigg|_{z=d^{-}} = \varepsilon_{H} \sum_{j=1}^{N} a_{ij}^{(1)} \phi_{j} \bigg|_{z=d^{+}}, \tag{37}$$

$$\sum_{j=1}^{N} \delta_{ij} H_j \bigg|_{z=d^-} = k_H \sum_{j=1}^{N} \delta_{ij} H_j \bigg|_{z=d^+}$$
(38)

Lastly, the following is the application of the Block-marching technique in Eqs. (21-26) into the halide perovskite layer governing Eqs. (1-7):

For a halide perovskite layer:

$$\sum_{j=1}^{L} \overline{a}_{ij}^{(1)} H_j + \frac{1}{e} \times \sum_{j=1}^{N} a_{ij}^{(1)} J_{H_j} + \frac{\sum_{k=1}^{N} \delta_{ik} E_k \sum_{j=1}^{N} \delta_{ij} H_j}{\tau_H \sum_{k=1}^{N} \delta_{ik} E_k + \tau_E \sum_{j=1}^{N} \delta_{ij} H_j} = G,$$
(39)

$$\sum_{j=1}^{N} \delta_{ij} J_{H_j} + e \times D_{H_{halide}} \left(\sum_{j=1}^{N} a_{ij}^{(1)} H_j + \frac{1}{V_T} \sum_{k=1}^{N} \delta_{ik} H_k \sum_{j=1}^{N} a_{ij}^{(1)} \phi_j \right) = 0, \tag{40}$$

$$\sum_{j=1}^{L} \overline{a}_{ij}^{(1)} E_j - \frac{1}{e} \times \sum_{j=1}^{N} a_{ij}^{(1)} J_{E_j} + \frac{\sum_{k=1}^{N} \delta_{ik} E_k \sum_{j=1}^{N} \delta_{ij} H_j}{\tau_H \sum_{k=1}^{N} \delta_{ik} E_k + \tau_E \sum_{i=1}^{N} \delta_{ij} H_j} = G, \tag{41}$$

$$\sum_{j=1}^{N} \delta_{ij} J_{E_j} - e \times D_{E_{halide}} \left(\sum_{j=1}^{N} a_{ij}^{(1)} E_j - \frac{1}{V_T} \sum_{k=1}^{N} \delta_{ik} E_k \sum_{j=1}^{N} a_{ij}^{(1)} \phi_j \right) = 0, \tag{42}$$

$$\sum_{j=1}^{L} \overline{a}_{ij}^{(1)} I_j + \sum_{j=1}^{N} a_{ij}^{(1)} F_{I_j} = 0, \tag{43}$$

$$\sum_{j=1}^{N} \delta_{ij} F_{I_j} + D_I \left(\sum_{j=1}^{N} a_{ij}^{(1)} H_j + \frac{1}{V_T} \times \sum_{k=1}^{N} \delta_{ik} I_k \times \sum_{j=1}^{N} a_{ij}^{(1)} \phi_j \right) = 0, \tag{44}$$

$$\sum_{j=1}^{N} a_{ij}^{(2)} \phi_j + \frac{e}{\varepsilon_p} \sum_{j=1}^{N} \delta_{ij} I_j = \frac{e}{\varepsilon_p} \times N_0,$$
 (45)

Iterative technique

The iterative technique is used to solve the nonlinearity problem^{37,40,41}. Firstly, this technique solved the equations as linear, thus, solved them as nonlinear with apply the convergence form such^{37,40,41}:

$$\left| \frac{E_{s+1}}{E_s} \right| < 1, \quad \left| \frac{H_{s+1}}{H_s} \right| < 1, \quad \left| \frac{I_{s+1}}{I_s} \right| < 1, \quad \text{where s} = 0, 1, 2, \dots$$
 (46)

Then, Discrete singular convolution differential quadrature (DSC-DQ) method combined with the technique of block-marching to analyze the problem at $\alpha \in]0,1[$ and $\beta \in]1,2[$. This work delves into the realm of fractional derivatives, a mathematical concept characterized by diverse definitions. This study will focus on the Caputo fractional derivative, widely recognized as the most prevalent definition within the field.

Caputo's fractional derivative

Building upon the foundation of the Riemann–Liouville fractional derivative⁵⁶, Caputo introduced a novel definition for fractional derivatives. This definition, now widely recognized as the Caputo fractional derivative, is formally expressed in the following equation, as detailed by Weilbeer⁵⁷.

If $\lambda \in R^+$, where " κ " is a positive integer and $\kappa - 1 < \lambda < \kappa$, the Riemann–Liouville fractional derivative of order λ (α , β) for a function u (t) is defined as:

$$D_a^{\lambda} u(t) = \frac{1}{\Gamma(\kappa - \lambda)} \frac{d^{\kappa}}{dt^{\kappa}} \int_a^t (t - z)^{\kappa - \lambda - 1} u^{\kappa}(z) dz, \tag{47}$$

The Caputo fractional derivative, a refinement of the Riemann–Liouville approach, involves a distinct computational procedure. Unlike direct fractional differentiation, the Caputo method first applies an integer-order derivative to the function and then performs fractional-order integration. This approach offers several advantages, particularly when dealing with functions that have initial conditions involving integer-order derivatives.

$$D_a^{\lambda} u(t) = \begin{cases} \frac{1}{\Gamma(\kappa - \lambda)} \int_a^t (t - z)^{\kappa - \lambda - 1} u^{\kappa}(z) dz, & \kappa - 1 < \lambda < \kappa \\ \frac{d^{\kappa} u}{dt^{\kappa}}, & \kappa = \lambda \end{cases}$$
(48)

The notation $D^{\lambda}_{\alpha}u\left(t\right)$ denotes the Caputo fractional derivative of order λ of the function $u\left(t\right)$ with respect to time (t), where the integration commences at the point "a". This derivative provides a generalized representation of how the function $u\left(t\right)$ evolves over time, extending beyond the conventional concept of integer-order derivatives.

When $\lambda = \kappa$, the Caputo fractional derivative reduces to the standard integer-order derivative.

Numerical results

Differential quadrature method is employed by using discrete singular convolution shape function to analyze the performance of a halide perovskite solar cell composed with electron and hole transport layers (PCBM/CH3NH3GeI3/CuI). The results are compared with previous experimental studies and prove high accuracy and efficiency with error of 10^{-8} .

Common materials proprities used in this model are taken from previous experimental studies $^{32,34-36,42-45}$ as shown in Table 1.

(a) Delta lagrange kernel (DLK):

Table 2 indicates that the values of current density (J) matches with other previous studies with the increase in grid points ($3 \le N \le 11$). At $N \ge 7$, the results approve the experiment ^{32,58,59}, numerical ^{37–45}, SCAPS-1D^{42,43}, and theoretical ³² results, at 11.84 sec time of performance.

(b) Regularized shannon kernel (RSK):

By changing the value of regularization factor (σ) from $[1.0h_z]$ to $[2.25h_z]$, the results match with previous experiment 30,32,60 , numerical $^{37-45}$, SCAPS-1D simulator 42,43 , and theoretical 32 studies at grid points ≥ 7 , time of performance 8.15 s, band width $2M+1\geq 3$, $\sigma=2.25h_z$, and error of 10^{-8} .

So, the ksernel of Regularized Shannon reaches the accurate results faster than Delta Lagrange because lower grid ponts and performance time. Hence, it is the most efficient kernel for investigating the halide perovskite layer composed between ETL and HTL performance and PCE. The results through Tables 2, 3, 4 are obtained at conditions:

$$L_E = 100 \text{ nm}, \, L_H = 200 \text{ nm}, \, \tau_E = 3 \text{ ns}, \, \tau_H = 300 \text{ ns} \,\, D_E = 10^{-5} \text{m}^2 s^{-1}, \, D_H = 10^{-6} \,\, \text{m}^2 s^{-1}, \, D_I = 10^{-17} \,\, \text{m}^2 s^{-1}, T = 300 \, \text{k}$$

The number of blocks has been changed with time as shown in Table 5 to indicate the suitable number which will give high accuracy. Table 5 shows that the values of fill factor (FF %) and power conversion efficiency (PCE %) matches with previous experimental results at $\Delta t=1$ s, and $time\,levels$ number $(\ell=4)$ above block number ≥ 12 and 8.3 s time of performance.

In order to calculate the Fill factor percentage (FF %) we use the following relation⁶¹:

$$FF\% = \frac{V_m J_m}{V_{cool} J_{coo}} \times 100 \tag{49}$$

So, the efficiency can be presented as follow⁶¹:

$$PCE\% = \frac{P_{\text{max}}}{P_{in}} \times 100 = \frac{V_{\text{max}} J_{\text{max}}}{J A} \times 100 = \frac{FF \ V_{oc} \ J_{sc}}{J \ A}$$
 (50)

where J represents solar radiation intensity and A denotes the area.

Table 6 shows that the values of fill factor (FF %) and power conversion efficiency (PCE %) matches with previous experimental results at $\Delta t = 1$ s, and $time\ levels$ number ($\ell = 8$) for more than or equal 7 blocks

Symbol	$V_T({ m V})$	ε	e(C)	T(k)	D(nm)	B_n, B_p (ev)	$\varepsilon_0(F/m)$	E _{gap} (V)	$N_c,Nv \ (m^{-3})$	$D_H, D_E \ (\mathrm{m}^2\mathrm{s}^{-1})$	$\alpha({ m m}^{-1})$
Value	25.7×10^{-3}	$10 \varepsilon_0$	1.6*10-19	300	250	0	2.7*10-11	1.5	1019	1.7×10^{-4}	1.3×10 ⁷

Table 1. The common parameters used for a halide perovskite inserted between electron and hole transport layers.

	Halide perovskite thickness (nm)								
Method	100	200	400	600	800	1000			
DSC-DQ (DLK)									
N=3	82.444	115.241	146.157	155.983	155.001	153.840			
N=5	79.111	112.780	142.005	153.854	152.423	151.777			
N=7	78.247	111.225	141.157	152.747	151.984	150.571			
N=9	78.247	111.225	141.157	152.747	151.984	150.571			
N=11	78.247	111.225	141.157	152.747	151.984	150.571			
Experiment results ^{30,32,60}	78.247	111.225	141.157	152.747	151.984	150.571			
Theoretical results ³²	78.247	111.225	141.157	152.747	151.984	150.571			
SCAPS-1D simulator ^{42,43}	78.247	111.225	141.157	152.747	151.984	150.571			
Time of performance	11.84 (second) – uniform grids ≥ 7								

Table 2. Current Density in Halide Perovskites: Thickness Dependence Analyzed by DSC-DQ with DLK at Varying Grid Points (N), Compared to Prior Studies ($\alpha = 1$ and $\beta = 2$).

		Regularization factor (σ)									
N	2 M+1	1.0 Hz	2.0 Hz	2.1 Hz	2.15 Hz	2.25 Hz					
	3	163.789	160.444	158.457	156.058	155.983					
3	5	163.789	160.444	158.457	156.058	155.983					
	7	163.789	160.444	158.457	156.058	155.983					
	3	160.217	158.473	156.257	154.005	153.854					
5	5	160.217	158.473	156.257	154.005	153.854					
	7	160.217	158.473	156.257	154.005	153.854					
	3	158.777	154.111	153.221	153.001	152.747					
7	5	158.777	154.111	153.221	153.001	152.747					
	7	158.777	154.111	153.221	153.001	152.747					
	3	158.777	154.111	153.221	153.001	152.747					
9	5	158.777	154.111	153.221	153.001	152.747					
	7	158.777	154.111	153.221	153.001	152.747					

Table 3. Variation of current density (A/m²) using DSC-DQ Method with RSK at several band width, grid point, and regularization factor at L = 600 nm and ($\alpha = 1$ and $\beta = 2$).

	Halide perovskite thickness (nm)								
Method	100	200	400	600	800	1000			
DSC-DQ (RSK)									
N = 3	80.579	113.470	142.927	154.053	152.997	152.009			
N=5	79.291	112.479	142.471	153.753	152.423	151.127			
N=7	78.247	111.225	141.157	152.747	151.984	150.571			
N=9	78.247	111.225	141.157	152.747	151.984	150.571			
N=11	78.247	111.225	141.157	152.747	151.984	150.571			
Experiment results ^{30,32,60}	78.247	111.225	141.157	152.747	151.984	150.571			
Theoretical results ³²	78.247	111.225	141.157	152.747	151.984	150.571			
SCAPS-1D simulator ^{42,43}	78.247	111.225	141.157	152.747	151.984	150.571			
Time of performance	8.15 (second) – uniform grids ≥ 7								

Table 4. Current Density in Halide Perovskites: Thickness Dependence Analyzed by DSC-DQ with RSK at Varying Grid Points (N), Compared to Prior Studies $(2M+1=3,\sigma=2.25h_z,\alpha=1)$ and $\beta=2$.

	No. of blocks					No. of blocks				
Time (s)	1	6	12	Experiment ^{30,32,60}	1	6	12	Experiment ^{30,32,60}		
0	47.14	46.22	45.276	45.27	15.25	14.88	14.455	14.45		
50	61.32	60.51	60.223	60.2	18.005	17.321	17.001	17		
100	61.995	60.987	60.784	60.78	17.980	17.542	17.201	17.2		
150	65.954	65.451	65.222	65.2	18.980	18.123	18.005	18		
200	66.897	66.457	66.308	66.3	19.215	18.745	18.623	18.6		
250	67.749	67.189	67.008	67	19.762	19.238	19.004	19		
300	69.001	68.682	68.500	68.5	19.789	19.476	19.311	19.3		
350	70.777	70.412	70.205	70.2	20.051	19.995	19.807	19.8		
400	71.267	70.912	70.712	70.7	20.541	20.230	20.052	20.05		
Performance time 8.3 (second) – over no. of blocks ≥ 12										

Table 5. Variation of Fill factor (FF) and efficiency (PCE) with time using DSC-DQ Method based on RSK at

	FF % No. of blocks					PCE % No. of blocks				
Time (s)	1	5	7	Experiment ^{30,32,60}	1	5	7	Experiment ^{30,32,60}		
0	45.444	45.301	45.276	45.27	14.622	14.561	14.455	14.45		
50	60.435	60.311	60.223	60.2	17.266	17.109	17.001	17		
100	60.98	60.845	60.784	60.78	17.345	17.261	17.201	17.2		
150	65.379	65.245	65.222	65.2	18.187	18.100	18.005	18		
200	66.379	66.322	66.308	66.3	18.721	18.655	18.623	18.6		
250	67.138	67.015	67.008	67	19.199	19.087	19.004	19		
300	68.612	68.525	68.500	68.5	19.487	19.328	19.311	19.3		
350	70.329	70.222	70.205	70.2	19.867	19.820	19.807	19.8		
400	70.788	70.725	70.712	70.7	20.125	20.074	20.052	20.05		
Performance time	7.1 (second) – over no. of blocks ≥ 7									

Table 6. Variation of Fill factor (FF) and efficiency (PCE) with time using DSC-DQ Method based on RSK at

and within 7.1 s of execution time. So, more time levels in the block (ℓ = 8) lead to analyze the performance and PCE of composite solar cells with more efficient and accuracy.

Table 7 shows that the values of fill factor (FF %) and power conversion efficiency (PCE %) matches with previous experimental results at $\alpha=0.9,\ \beta=1.75$ over number of blocks ≥ 7 and within 7.1 s of execution time. So, reducing the fractional orders lead to analyze the performance and PCE of composite solar cells with more efficient and accuracy. Tables 5, 6, 7 indicate that block marching technique depends on choosing suitable $(\Delta t, \ell, \alpha, \beta)$ in order to get high efficiency and accuracy results.

Tables 2, 6, 7 proved that this method is an efficient and accurate method for analyzing the performance of halide perovskite layer composed between ETL and HTL at (number of blocks \geq 3, N \geq 7, 2M+1 \geq 3, σ = 2.25 h_x , Δ T = 1 s, ℓ = 8, α = 0.9, β = 1.75 and performance time=5 s). This methodology is subsequently employed to conduct a parametric study investigating the influence of mobilities (μ_E , μ_H), energy gap (E_{gap}), ETL, HTL, halide perovskite thicknesses (L_E , L_H , L), and temperatures (T) on current density (J), Fill factor (FF%) open circuit voltage (V_{oc}) and efficiency (PCE) of a composite solar cell.

Figure 2 show the vital role that temperature, ETL thickness, and HTL thickness play to change the current density (J) value. So, increasing the temperature leads to increase the current density as shown in Fig. 2. Also, increasing HTL thickness leads to increase the current density, but increasing ETL thickness leads to decrease the current density. To get high current density, we should use low ETL thickness nearly $L_{\rm E}$ = 50 nm and high HTL thickness nearly $L_{\rm H}$ = 300 nm at high temperature over 500 k.

Also, Fig. 3 show the vital role that temperature, ETL thickness, and HTL thickness play to change the open circuit voltage (V_{oc}) value. So, increasing the temperature leads to decrease the open circuit voltage. Increasing HTL thickness leads to increase the open circuit voltage, but increasing ETL thickness leads to decrease the open circuit voltage. To achieve high open-circuit voltage, it is recommended to utilize a thin Electron Transport Layer (ETL) with a thickness of approximately 50 nm, coupled with a thicker Hole Transport Layer (HTL) of approximately 300 nm, while operating at a low temperature of around 250 K.

Figure 4 show how the temperature, ETL thickness, and HTL thickness effect on changing the Fill factor (FF %) value. So, increasing the temperature leads to decrease the Fill factor as shown in Fig. 4. Also, increasing HTL thickness leads to decrease the Fill factor, but increasing ETL thickness leads to increase the Fill factor. So, to

	FF %				PCE % No. of blocks				
	No. of b	locks							
Time (s)	1	5	7	Experiment ^{30,32,60}	1	5	7	Experiment ^{30,32,60}	
0	45.294	45.281	45.276	45.27	14.467	14.457	14.455	14.45	
50	60.243	60.233	60.223	60.2	17.110	17.008	17.001	17	
100	60.881	60.789	60.784	60.78	17.235	17.206	17.201	17.2	
150	65.254	65.225	65.222	65.2	18.105	18.008	18.005	18	
200	66.311	66.309	66.308	66.3	18.625	18.624	18.623	18.6	
250	67.021	67.010	67.008	67	19.099	19.006	19.004	19	
300	68.552	68.502	68.500	68.5	19.324	19.315	19.311	19.3	
350	70.212	70.207	70.205	70.2	19.811	19.809	19.807	19.8	
400	70.716	70.714	70.712	70.7	20.111	20.074	20.052	20.05	
Performance time	nance time $ $ 5 (second) – over no. of blocks ≥ 7								

Table 7. Variation of Fill factor (FF) and efficiency (PCE) with time using DSC-DQ Method based on RSK at

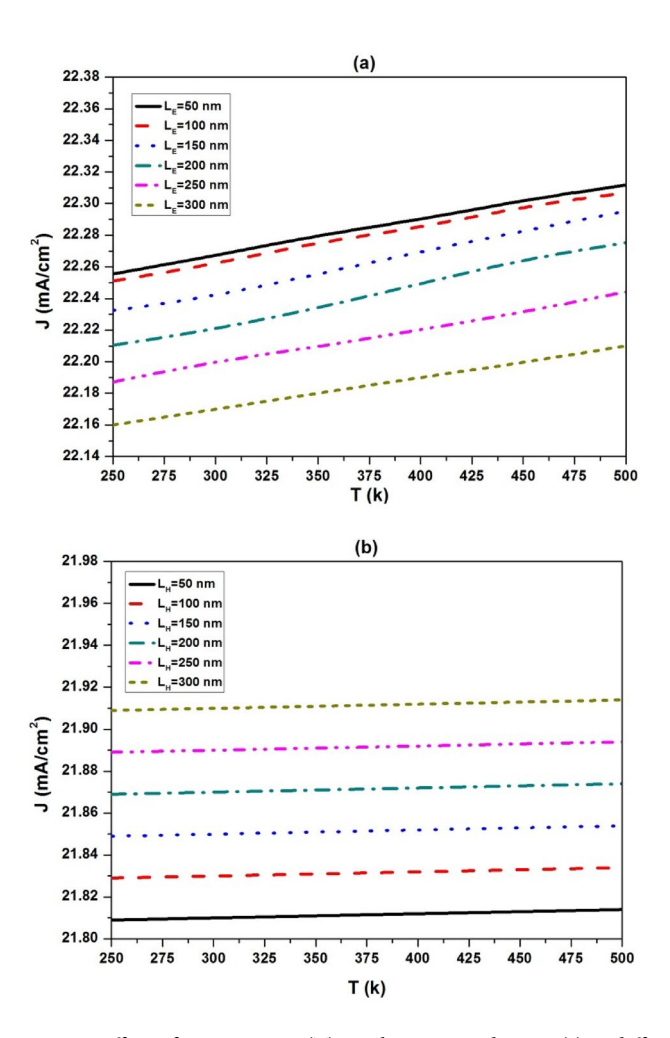


Fig. 2. Effect of temperature (T) on the current density (J) at different thicknesses of (a) electron transport layer (L_E) and (b) hole transport layer (L_H) for PCBM/CH3NH3GeI3/CuI solar cell at $L=400\,nm$, $E_{gap}=1.5$ eV, $\tau_E=3$ ns, $\tau_H=300$ ns, $D_E=10^{-5} {\rm m}^2 s^{-1}$, $D_H=10^{-6} {\rm m}^2 s^{-1}$, $D_I=10^{-17} {\rm m}^2 s^{-1}$.

get high Fill factor value, we should use high ETL thickness nearly $L_{\rm E}$ = 300 nm and low HTL thickness nearly $L_{\rm H}$ = 50 nm at low temperature about 250 k.

For Power Conversion Efficiency (PCE %) Fig. 5 show the effect temperature, ETL thickness, and HTL thickness on changing the Power Conversion Efficiency (PCE %) value. Increasing the temperature leads to

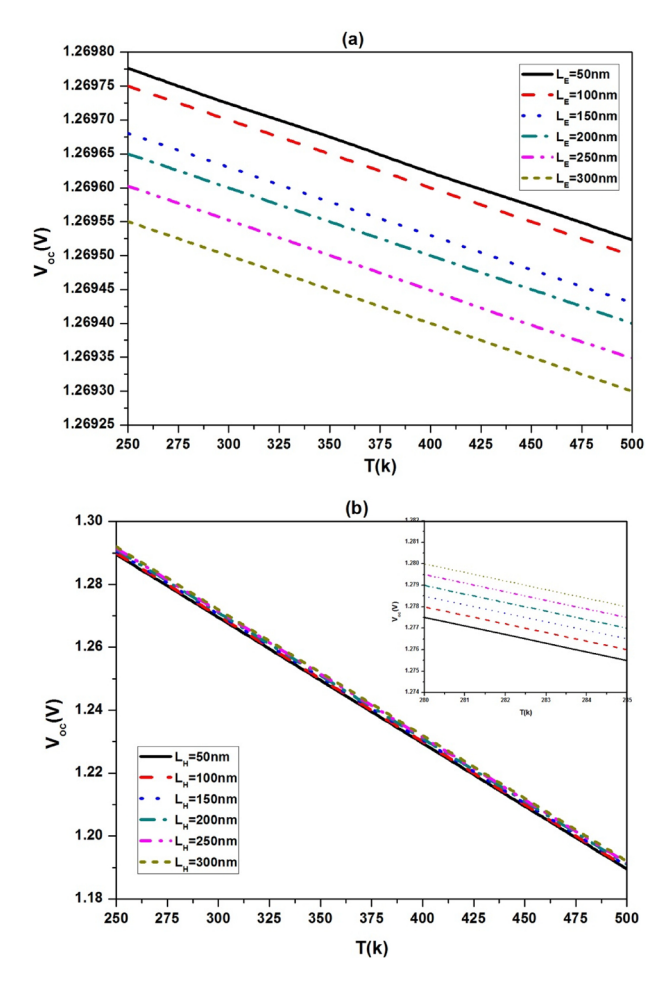


Fig. 3. Effect of temperature (T) on the open circuit voltage (V $_{oc}$) at different thicknesses of (a) electron transport layer (L $_{E}$) and (b) hole transport layer (L $_{H}$) for PCBM/CH3NH3GeI3/CuI solar cell at $L=400\,nm,~E_{gap}=1.5~{\rm eV},~\tau_{E}=3~{\rm ns},~\tau_{H}=300~{\rm ns},~D_{E}=10^{-5}{\rm m}^{2}s^{-1},~D_{H}=10^{-6}{\rm m}^{2}s^{-1},D_{I}=10^{-17}{\rm m}^{2}s^{-1}$.

decrease the Power Conversion Efficiency as shown in Fig. 5. Also, increasing HTL thickness and ETL thickness lead to decrease the Power Conversion Efficiency. So, to get high Power Conversion Efficiency value for this composite solar cell, we should use low thickness for ETL and HTL nearly (LE=LH=50 nm) at low temperature about 250 k.

Figure 6 illustrates the critical influence of halide perovskite absorber layer thickness on key photovoltaic parameters: open-circuit voltage (Voc), fill factor (FF), current density (J), and power conversion efficiency (PCE). Analysis reveals that increasing the halide layer thickness generally leads to a decrease in open-circuit voltage and fill factor, while simultaneously increasing current density and power conversion efficiency.

Finally, Fig. 7 illustrate the influence of different mobilities and gap energies on the current density (J), the open circuit voltage (Voc), the Fill factor (FF %), and the Power Conversion Efficiency (PCE %) values. It is noticed that the increase in electron and hole mobilities lead to decrease open circuit voltage, but increase the Fill factor, the current density, and the Power Conversion Efficiency. Also, the increase in gap energy leads to increase open circuit voltage, but decrease the Fill factor, the current density, and the Power Conversion Efficiency. So, to get high Fill factor, current density and Power Conversion Efficiency, we should use high mobilities at low gap energy as shown in Fig. 7, but low mobilities at high gap energy to get high open circuit voltage.

Figure 8 illustrates the dependence of current density variance on voltage for different ETL and HTL thicknesses, respectively. As the ETL thickness increased, a general trend of reduced variance at higher voltages was observed, suggesting improved charge transport efficiency. For instance, at 0.8 V, the variance for ETL thicknesses of 50 nm, 100 nm, and 150 nm was approximately 0.25 mA²/cm⁴, 0.15 mA²/cm⁴, and 0.10 mA²/cm⁴, respectively. This indicates that a thicker ETL facilitates more consistent charge extraction and reduces recombination losses.

In contrast, increasing HTL thickness showed a more complex relationship, with an optimal thickness yielding the lowest variance. At 0.8 V, HTL thicknesses of 30 nm, 60 nm, and 90 nm resulted in variances of about $0.20 \text{ mA}^2/\text{cm}^4$, $0.08 \text{ mA}^2/\text{cm}^4$, and 0.12 m3.

A²/cm⁴, respectively. This suggests that while very thin or very thick HTLs can lead to imbalances or increased recombination, a mid-range thickness optimally supports balanced charge extraction.

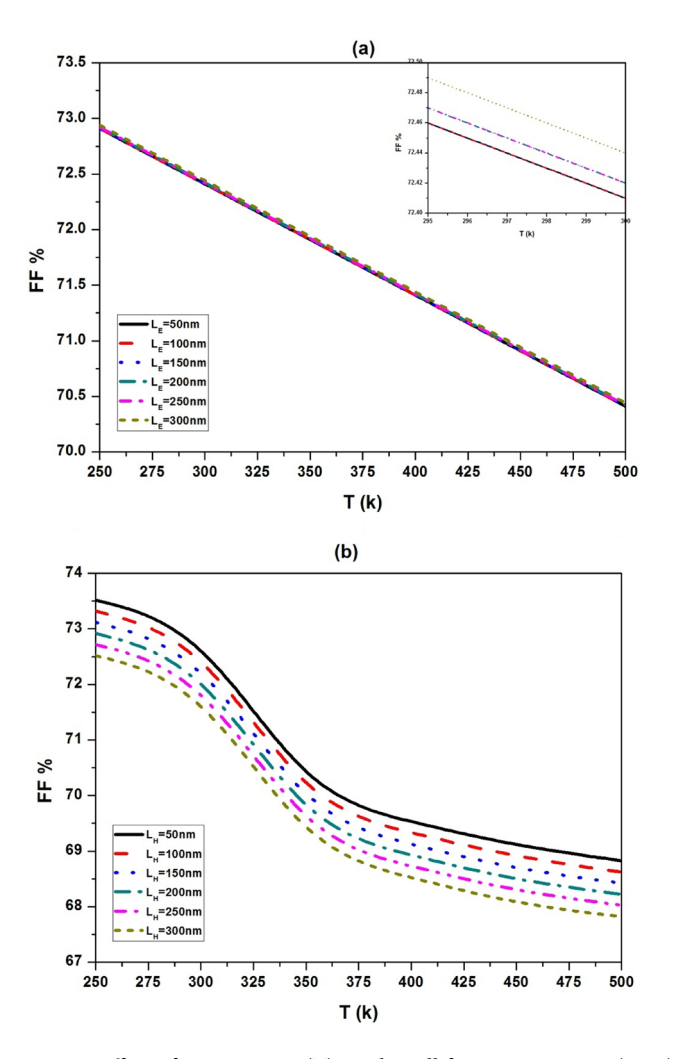


Fig. 4. Effect of temperature (T) on the Fill factor percentage (FF%) at different thicknesses of (a) electron transport layer (L_E) and (b) hole transport layer (L_H) for PCBM/CH3NH3GeI3/CuI solar cell at $L=400\,nm$, $\rm E_{gap}=1.5$ eV, $\tau_E=3$ ns, $\tau_H=300$ ns, $\rm D_E=10^{-5}m^2s^{-1}$, $\rm D_H=10^{-6}m^2s^{-1}$, $\rm D_I=10^{-17}m^2s^{-1}$.

The analysis demonstrates that both ETL and HTL thicknesses play vital roles in determining the uniformity and efficiency of current transport in perovskite solar cells. Optimizing these thicknesses can lead to significant improvements in device stability and performance.

- Figure 8-a: Simulated graph showing the effect of varying ETL thickness (30 nm, 50 nm, 100 nm, 150 nm, 200 nm) on current density variance with voltage (0–1.2 V). The graph shows that as ETL thickness increases, the current density variance consistently decreases across the voltage range, indicating improved charge extraction and reduced recombination with thicker ETLs.
- Figure 8-b Simulated graph showing the effect of varying HTL thickness (20 nm, 40 nm, 60 nm, 80 nm, 100 nm) on current density variance with voltage. At 0.8 V, the variance is lowest for 60 nm, suggesting an optimal HTL thickness that balances charge mobility and recombination.

Figure 9 presents the J-V curves of the perovskite solar cell at different temperatures for two different gap energies: (a) $E_{\rm gap}=1.55~{\rm eV}$ and (b) $E_{\rm gap}=1.35~{\rm eV}$. The figure clearly shows the impact of temperature on the J-V curves. As temperature increases, both the short-circuit current (Jsc) and the open-circuit voltage (Voc) decrease. This is consistent with the expected behavior of solar cells, as higher temperatures generally lead to increased thermal losses and reduced efficiency. Comparing the two plots, we can observe the effect of gap energy on the J-V curves. The shape of the curves and the magnitude of Jsc and Voc are different for the two gap energies. This highlights the importance of tuning the gap energy to optimize solar cell performance.

Discussion

Current high efficiency levels and proposes a feasible experimental scheme

While our paper primarily focuses on the application of the FDQ method to accurately simulate perovskite solar cell performance, the simulation results provide a strong foundation for future optimization strategies. Based on our findings, we propose the following optimization directions:

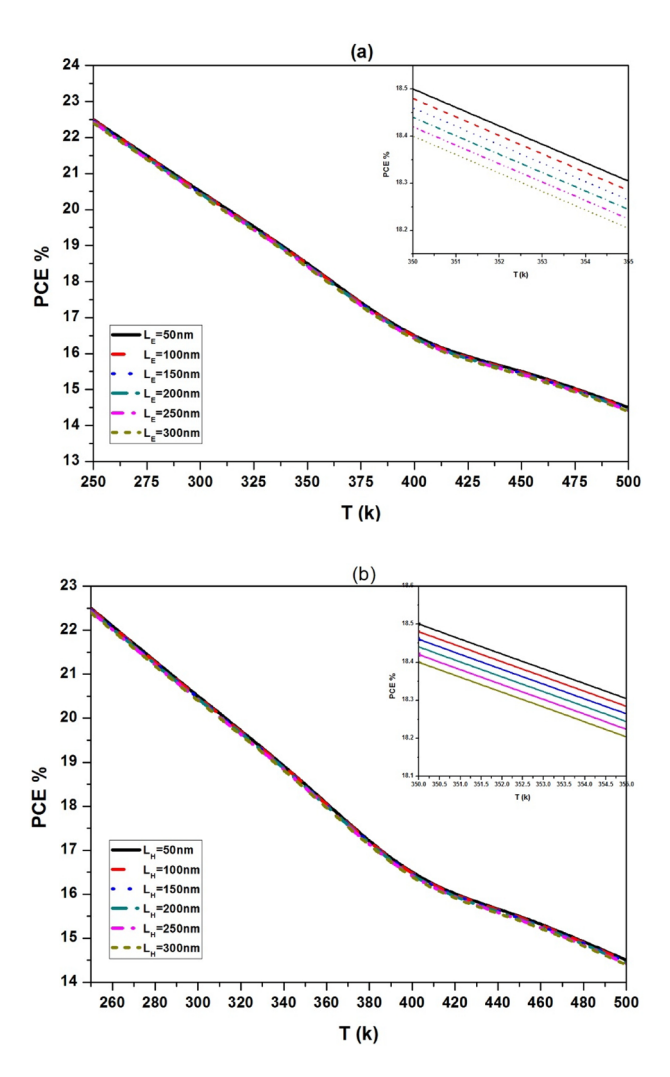


Fig. 5. Effect of temperature (T) on the Power Conversion Efficiency (PCE %) at different thicknesses of (a) electron transport layer (L_E) and (b) hole transport layer (L_H) for PCBM/CH3NH3GeI3/CuI solar cell at $L=400\,nm$, $E_{gap}=1.5$ eV, $\tau_E=3$ ns, $\tau_H=300$ ns, $D_E=10^{-5} \mathrm{m}^2 s^{-1}$, $D_H=10^{-6} \mathrm{m}^2 s^{-1}$, $D_I=10^{-17} \mathrm{m}^2 s^{-1}$.

- Our parametric studies (e.g., as shown in Fig. 6 and Table 4 indicate that the device performance is highly dependent on parameters such as layer thickness and material properties. So, the future work will involve using optimization algorithms, in conjunction with our FDQ simulation, to identify the optimal combination of these parameters. This could include a sensitivity analysis to determine which parameters have the most significant impact on efficiency, allowing for a more targeted optimization approach.
- The model can be used to explore the impact of different materials for the ETL and HTL layers, in addition to the CH3NH3GeI3 absorber, to identify configurations that maximize efficiency.
- Further simulations will be designed to investigate the impact of interface modifications between the layers, which can significantly affect charge transport and recombination.

To validate these simulation-guided optimizations, we suggest the following experimental scheme:

- Fabricate devices with the optimized parameters identified through our simulations.
- Characterize the device performance (J-V curves, efficiency) and compare the results with our simulation predictions.
- Systematically vary the parameters around the optimized values to experimentally verify the sensitivity analysis.

While a precise prediction of the ultimate efficiency improvement is challenging without experimental validation, we believe this combined simulation-experimental approach will lead to significant progress in optimizing perovskite solar cell performance.

While the FDQ method offers several advantages, as highlighted in the paper (e.g., high accuracy, computational efficiency), it also has certain limitations:

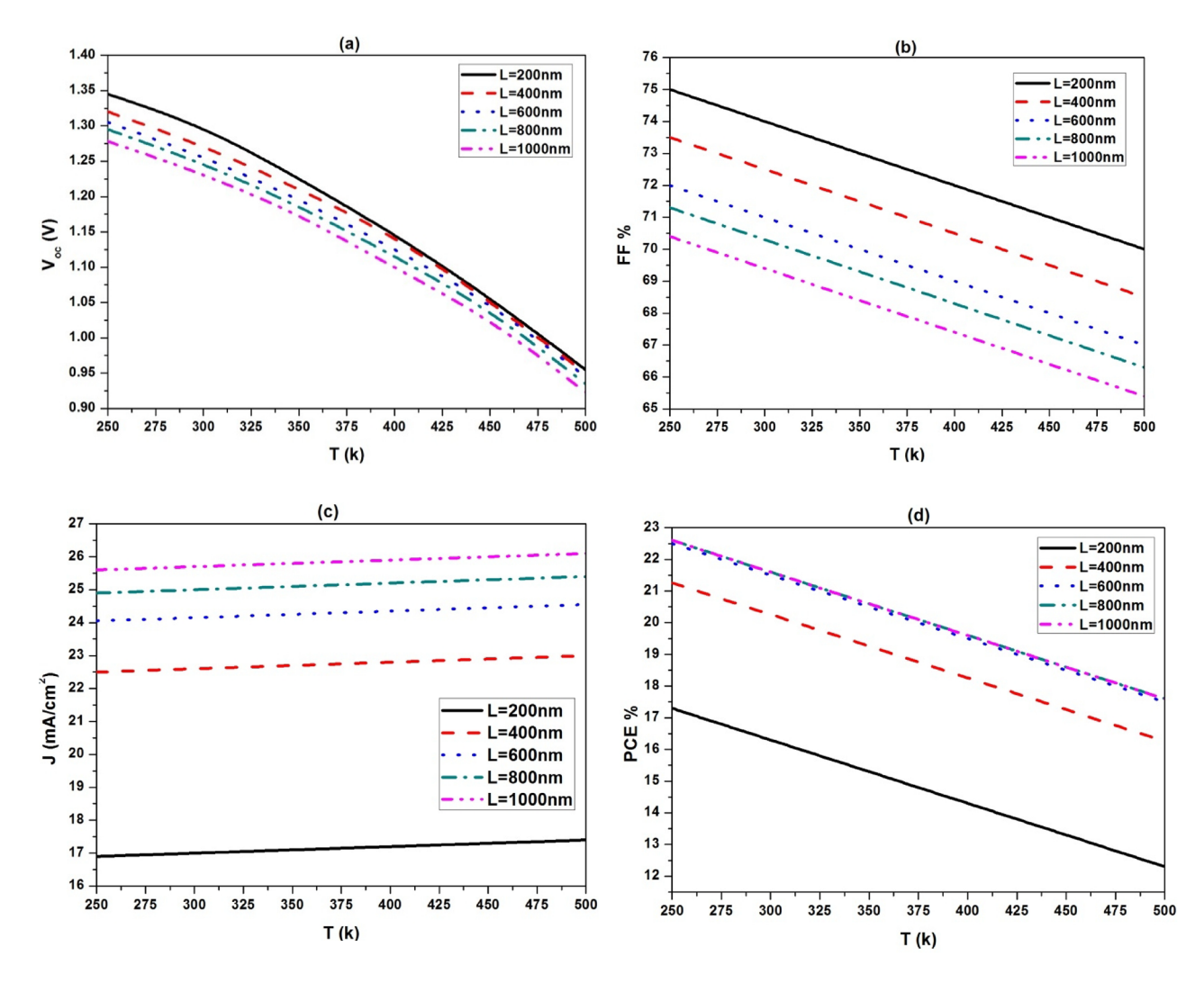


Fig. 6. Effect of temperature (T) and halide perovskite layer thickness (L) on (a) the open circuit voltage (V_{oc}), (b) the Fill factor (FF%), (c) the current density (J), and (d) the Power Conversion Efficiency (PCE %) $L_E = 200 \, nm$, $L_H = 150 \, nm$, $E_{gap} = 1.5 \, eV$, $\tau_E = 3 \, ns$, $\tau_H = 300 \, ns$, $D_E = 10^{-5} \, m^2 s^{-1}$, $D_H = 10^{-6} \, m^2 s^{-1}$, $D_I = 10^{-17} \, m^2 s^{-1}$.

- Like other global spectral methods, the computational cost of the FDQ method can increase significantly for
 problems with a large number of spatial dimensions. For very complex 3D simulations, other methods might
 become more efficient.
- Applying the FDQ method to problems with highly complex or irregular geometries can be challenging.
 Grid generation and implementation of boundary conditions can become more intricate compared to finite element or finite volume methods.
- While the FDQ method can be used for time-dependent problems, it might require careful selection of time
 integration schemes to ensure stability and accuracy. For certain highly transient problems, other methods
 might be preferred.
- The presence of strong singularities in the solution domain can reduce the accuracy of the FDQ method. Special techniques might be needed to handle such situations.

In the context of our perovskite solar cell simulations, we acknowledge that the current study focuses on 1D simulations. Extending the FDQ method to more complex 2D or 3D device structures would require addressing the computational cost and geometry limitations. We have added a discussion of these limitations to provide a more complete picture of the method's applicability.

Adjusting the bandgap experimentally

The paper focuses on modeling the performance of composite halide perovskite solar cells using the Fractional Differential Quadrature (FDQ) method. While the paper extensively discusses the impact of bandgap on the solar cell's efficiency, it does not detail experimental methods for adjusting the bandgap of CH3NH3GeI3. The paper's strength lies in its simulation and modeling, not in providing practical experimental synthesis procedures.

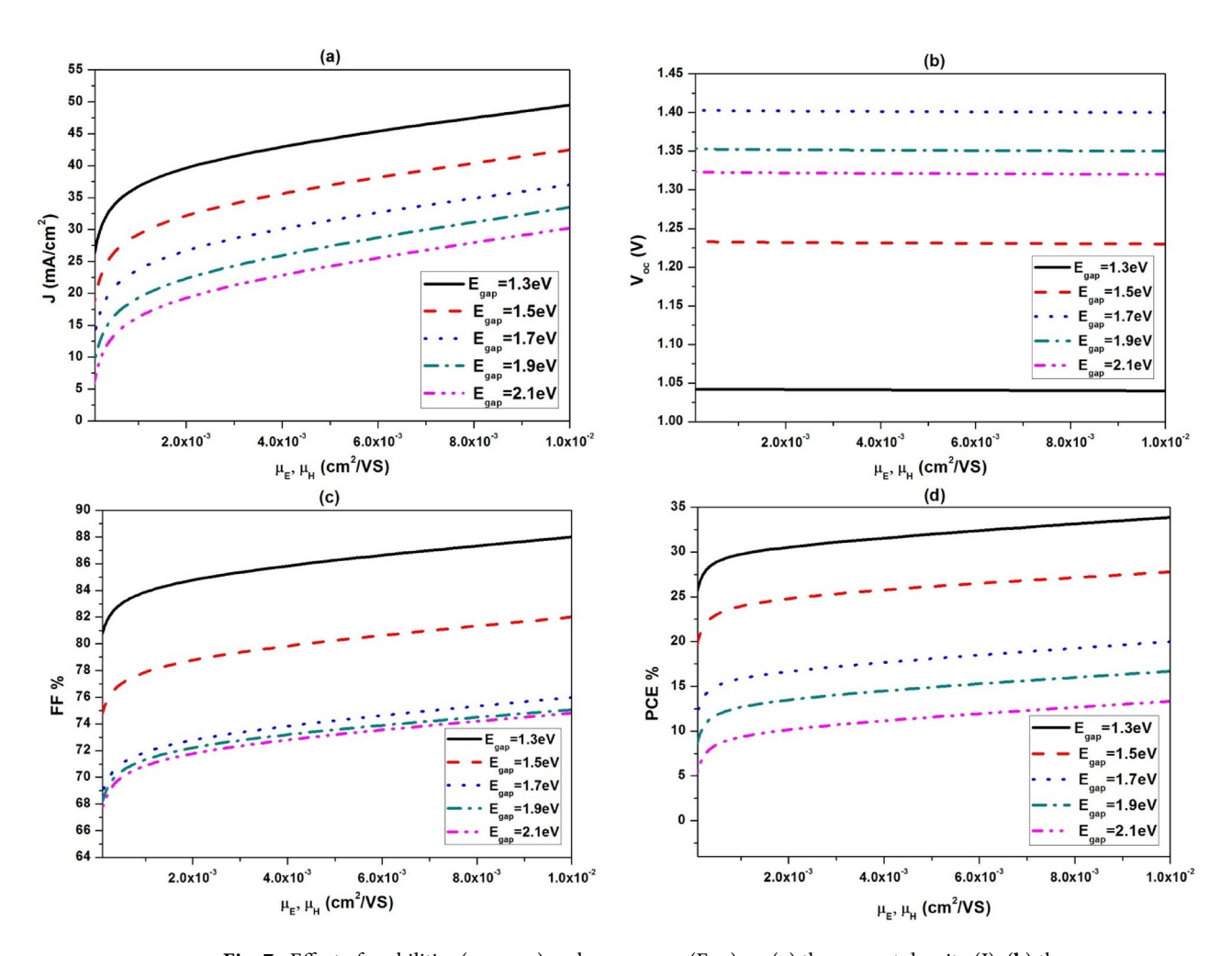


Fig. 7. Effect of mobilities (μ_E , μ_H) and gap energy ($E_{\rm gap}$) on (a) the current density (J), (b) the open circuit voltage ($V_{\rm oc}$), (c) the Fill factor (FF%), and (d) the Power Conversion Efficiency (PCE %) $L_E = 200\,n{\rm m}$, $L_H = 150\,n{\rm m}$, $L = 400\,n{m}$, $\tau_E = 3\,n{\rm m}$, $\tau_H = 300\,n{\rm m}$, $\tau_H = 10^{-5}{\rm m}^2{\rm s}^{-1}$, $\tau_H = 10^{-6}{\rm m}^2{\rm s}^{-1}$, $\tau_H = 10^{-6}{\rm m}^2{\rm s}^{-1}$.

To experimentally adjust the bandgap of CH3NH3GeI3, several approaches could be considered, though these are not explicitly described in the paper:

Methods to Adjust Bandgap:

- 1. Alloying/Mixed Halides: The most common method for bandgap engineering in perovskites is to create alloys by mixing different halides. For CH3NH3GeI3, this would involve partially substituting iodine (I) with other halides like bromine (Br) or chlorine (Cl). The resulting material would be CH3NH3GeI Rr or CH3NH3GeI Cl, where 'x' represents the molar fraction of the substituted halide. Increasing 'x' typically leads to a wider bandgap (higher energy). This requires careful control of the precursor ratios during synthesis.
- 2. Cation Engineering: Similar to halide substitution, the bandgap can be modified by partially substituting the organic cation ($CH_3NH_3^*$) with other organic or inorganic cations. This approach is more complex, potentially leading to changes in crystal structure and stability besides bandgap. The choice of substitute cation and its concentration would need careful consideration.
- 3. Quantum Dots: Synthesizing CH3NH3GeI3 quantum dots (QDs) allows for bandgap tunability through quantum confinement effects. The size of the QDs directly influences the bandgap; smaller QDs lead to a wider bandgap. However, this method requires specialized QD synthesis techniques.
- 4. Strain Engineering: Applying strain to the CH3NH3GeI3 film could potentially alter the bandgap. This is a more advanced technique requiring careful control of substrate choice and deposition methods.

Experimental Verification Scheme (building on the paper's suggestions :

The paper already suggests a verification scheme: fabricate devices with different bandgaps (achieved using one of the above methods), characterize their performance (J-V curves, efficiency), and compare the experimental results with the simulation predictions. A more detailed experimental plan would include:

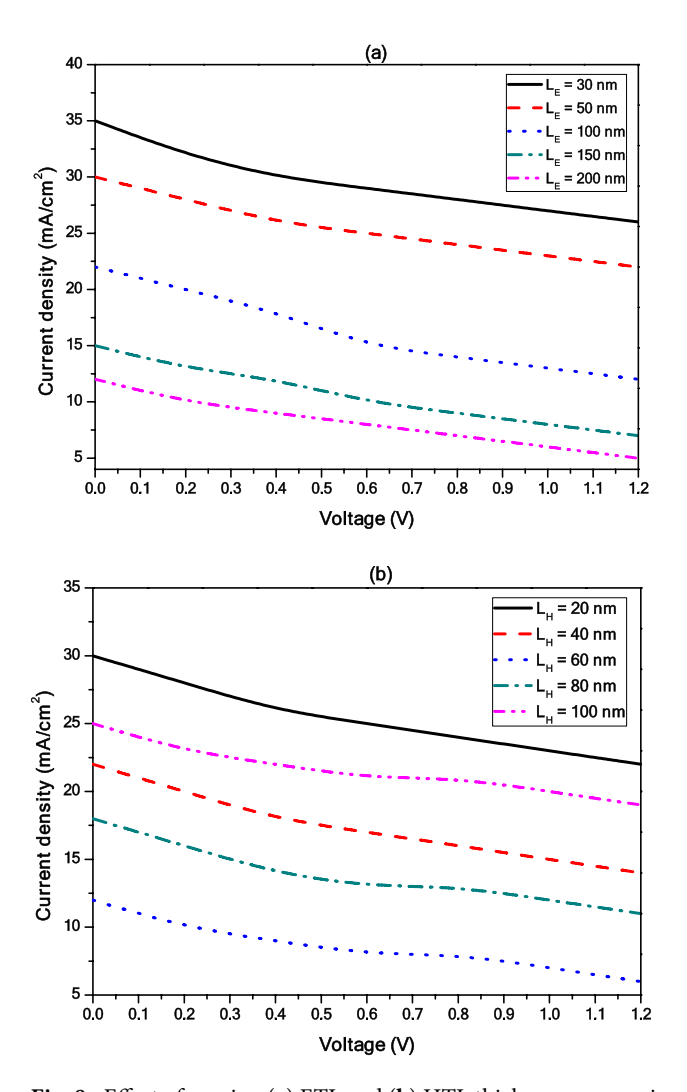


Fig. 8. Effect of varying (a) ETL and (b) HTL thicknesses on variance of the density of current with voltage at PCBM/CH3NH3GeI3/CuI solar $\mathbf{L} = 400 \, nm$, $\mathbf{E}_{gap} = 1.5 \, \text{eV}$, $\tau_E = 3 \, \text{ns}$, $\tau_H = 300 \, \text{ns}$, $\mathbf{D}_E = 10^{-5} \, \text{m}^2 \, \text{s}^{-1}$, $\mathbf{D}_H = 10^{-6} \, \text{m}^2 \, \text{s}^{-1}$, $D_I = 10^{-17} \, \text{m}^2 \, \text{s}^{-1}$.

- Synthesis: Precisely control the synthesis of CH3NH3GeI3 with varying halide or cation compositions (or QD size, if using that method). Techniques like solution-based methods (e.g., spin-coating) or vapor deposition could be employed. Careful characterization of the resulting films is crucial using techniques like X-ray diffraction (XRD) to confirm the crystal structure and composition, and UV-Vis spectroscopy to measure the bandgap.
- 2. Device Fabrication: Fabricate perovskite solar cells using the synthesized materials, incorporating the ETL (PCBM) and HTL (CuI) layers as described in the paper. Standard perovskite solar cell fabrication techniques would be used.
- Characterization: Measure the J-V characteristics of the fabricated devices under standard illumination conditions. Extract parameters like Jsc, Voc, FF, and PCE. Compare the experimental results with the FDQ simulation results for varying bandgaps.
- Further Analysis: Conduct additional characterizations like impedance spectroscopy and photoluminescence spectroscopy to gain deeper insights into charge transport and recombination processes at different bandgaps.

It's important to note that successfully modifying the bandgap while maintaining the stability and other desirable properties of the perovskite material is a significant challenge. The experimental work would require expertise in materials synthesis and characterization, as well as device fabrication techniques.

Hysteresis factor (HF)

To measure the amount of hysteresis in a device for a given voltage sweep method, we calculate a "hysteresis factor". This factor is determined by taking the absolute difference between the area under the forward-scan J-V curve and the area under the reverse-scan J-V curve, then dividing that result by the area under the reverse-scan curve.

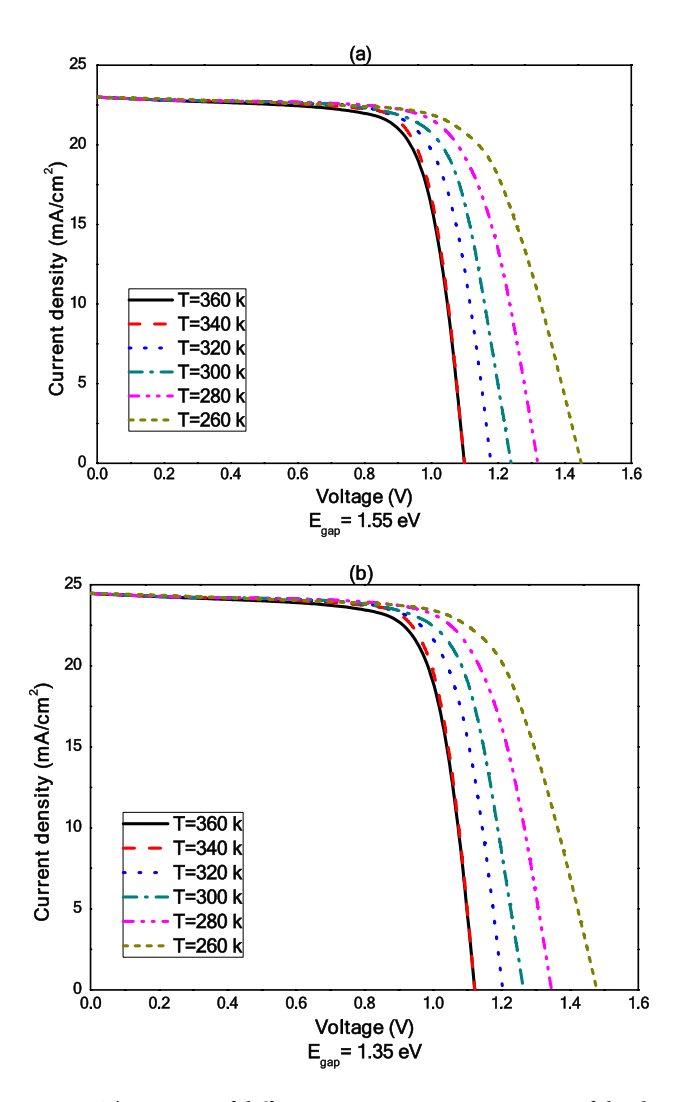


Fig. 9. The impact of different temperatures on variance of the density of current with voltage at different gap energies (a) $E_{gap}=1.55$ eV and b) $E_{gap}=1.35$ eV. $d=400\,nm$, $\tau_E=3$ ns, $\tau_H=300$ ns, $D_E=10^{-5}{\rm m}^2s^{-1}$, $D_H=10^{-6}{\rm m}^2s^{-1}$, $\mu_E=\mu_H=2\times10^{-4}cm^2/Vs$, $\Delta T=0.5$ s, L=12, and number of blocks =5

$$HF = \frac{A\left(|J_{reverse} - J_{forward}|\right)}{A\left(J_{reverse}\right)} \tag{51}$$

where $J_{reverse}$ and $J_{forward}$ are the non-negative current density for reverse and forward scan, respectively. A is the area under the curve determined by

$$j(V) = \max[J(V), 0] \text{ and } A(j) = \int_{V=0}^{V=V_{oc}} J(V) dV$$
 (52)

The open-circuit voltage $V_{\rm oc}$ is defined as the greater of the two values obtained from the reverse and forward J-V scans⁶². This approach ensures consistent evaluation, particularly when dealing with "inverted" hysteresis, where the forward scan's curve crosses or exceeds that of the reverse scan, as illustrated in Fig. 10

Conclusion

Differential quadrature method is employed by using discrete singular convolution shape function with (Delta Lagrange/Regularized Shannon) kernels to analyze the performance of a composite halide perovskite solar cell (PCBM/CH3NH3GeI3/CuI). The block-marching technique is produced to solve the time-dependent difficulty. These techniques help in transforming the nonlinear partial differential equations to system of nonlinear algebraic, then, we overcome the nonlinearity by applying the iterative method. With the aid of the MATLAB program, we obtain an efficient and accurate results compared with preceding experiment and numerical schemes. Discrete singular convolution differential quadrature method based on regularized shannon

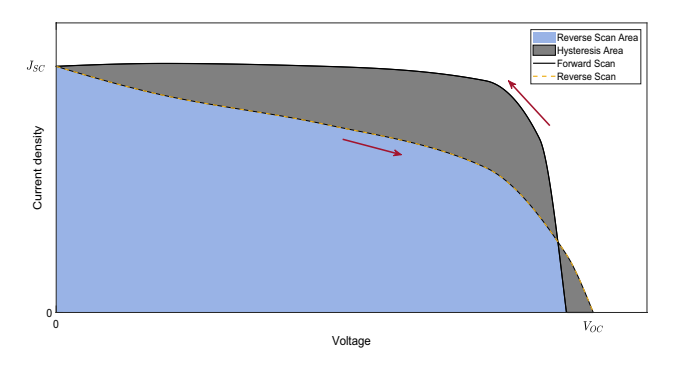


Fig. 10. Diagram showing the definition of the hysteresis factor (HF).

kernel with block marching proved that this method is an efficient and accurate method for analyzing the performance of halide perovskite layer composed between ETL and HTL at (number of blocks ≥ 3 , N ≥ 7 , $2M+1\geq 3,\sigma=2.25h_x$, $\Delta T=1$ s, $\ell=8$, $\alpha=0.9$, $\beta=1.75$ and performance time=5 s). Subsequently, we present a parametric study including the effects of temperature, thickness of various layers, mobilities, and energy gaps on power conversion efficiency, open circuit voltage, fill factor, and current density of composite halide perovskite solar cells. For all effects observed, it is noted that:

Fractional order models may provide a more accurate description of these transport processes compared to traditional integer-order models, potentially leading to improved predictions of PCE.

By incorporating fractional order derivatives into device models, researchers can gain a deeper understanding of trap state behavior and develop strategies to minimize their detrimental effects.

By incorporating fractional order derivatives into stability models, researchers can gain insights into the long-term performance and degradation mechanisms of these devices.

To maximize current density, it is generally beneficial to employ a thicker halide perovskite layer (approximately $L=1000~\rm nm$), a thinner Electron Transport Layer (ETL) with a thickness of around $LE=50~\rm nm$, and a thicker Hole Transport Layer (HTL) with a thickness of approximately $LH=300~\rm nm$, while operating at elevated temperatures exceeding 500 K.

To maximize open-circuit voltage, it is generally advantageous to utilize a thinner halide perovskite layer (approximately $L=200\,$ nm), a thinner Electron Transport Layer (ETL) with a thickness of around $LE=50\,$ nm, and a thicker Hole Transport Layer (HTL) with a thickness of approximately $LH=300\,$ nm, while operating at lower temperatures around 250 K.

To maximize fill factor (FF), it is generally advantageous to utilize a thinner halide perovskite layer (approximately L=200 nm), a thicker Electron Transport Layer (ETL) with a thickness of around LE=300 nm, and a thinner Hole Transport Layer (HTL) with a thickness of approximately LH=50 nm, while operating at lower temperatures around 250 K.

To maximize power conversion efficiency (PCE), it is generally advantageous to employ a thicker halide perovskite layer (approximately L=1000 nm), while simultaneously utilizing thinner Electron Transport Layers (ETL) and Hole Transport Layers (HTL), each with a thickness of around LE=LH=50 nm. Optimal PCE is typically achieved at lower operating temperatures, around 250 K.

To optimize device performance, a nuanced approach to carrier mobility is necessary. High carrier mobilities are generally desirable for enhancing fill factor (FF), current density (Jsc), and ultimately, power conversion efficiency (PCE), particularly within materials exhibiting low bandgap energies. Conversely, in materials with higher bandgap energies, lower carrier mobilities can contribute to an increase in open-circuit voltage (Voc).

It is expected that this method and their results are benefit for increasing the efficiency of solar cell energy. Future research should focus on experimentally validating the predictions of this model through physical fabrication and further investigations. The development of an extended time-dependent FDQ model, rigorously incorporating ion migration and capable of simulating hysteresis, is a crucial and promising direction for our future research efforts. Moreover, fractional order models offer a promising avenue for optimizing device parameters and material selection to achieve enhanced power conversion efficiency (PCE).

Data availability

Data is provided within the manuscript.

Received: 5 March 2025; Accepted: 16 June 2025 Published online: 22 August 2025

References

- 1. Yin, W., Pan, L., Yang, T. & Liang, Y. Recent advances in interface engineering for planar heterojunction perovskite solar cells. *Molecules* 21, 837 (2016).
- Ibn-Mohammed, T. et al. Perovskite solar cells: an integrated hybrid lifecycle assessment and review in comparison with other photovoltaic technologies. Renew. Sustain. Energy Rev. 80, 1321–1344 (2017).

- 3. Tang, H., He, S. & Peng, C. A short progress report on high-efficiency perovskite solar cells. Nanoscale Res. Lett. 12, 1-8 (2017).
- Shen, H. et al. Metal halide perovskite: a game-changer for photovoltaics and solar devices via a tandem design. Sci. Technol. Adv. Mater. 19, 53–75 (2018).
- 5. Dharmadasa, I. M., Rahaq, Y., Ojo, A. A. & Alanazi, T. I. Perovskite solar cells: a deep analysis using current-voltage and capacitance-voltage techniques. J. Mater. Sci.: Mater. Electron. 30, 1227–1235 (2019).
- Shi, Z. & Jayatissa, A. H. Perovskites-based solar cells: a review of recent progress, materials and processing methods. Materials. 11, 729 (2018).
- 7. Trivedi, S. et al. Recent progress in growth of single-crystal perovskites for photovoltaic applications. ACS Omega 6, 1030–1042 (2021).
- 8. Siegrist, S. et al. Triple-cation perovskite solar cells fabricated by a hybrid PVD/blade coating process using green solvents. *J. Mater. Chem. A.* **9**, 26680–26687 (2021).
- 9. Y.-H. Chiang, K. Frohna, H. Salway, A. Abfalterer, B. Roose, M. Anaya, S.D. Stranks, Efficient all-perovskite tandem solar cells by dual-interface optimisation of vacuum-deposited wide-bandgap perovskite, ArXiv Preprint ArXiv:2208.03556. (2022).
- 10. M.Y. Rahman, S.M. Mominuzzaman, Exploring Lead Free Mixed Halide Double Perovskites Solar Cell, ArXiv Preprint ArXiv:2401.09584. (2024).
- 11. Stoumpos, C. C., Malliakas, C. D. & Kanatzidis, M. G. Semiconducting tin and lead iodide perovskites with organic cations: phase transitions, high mobilities, and near-infrared photoluminescent properties. *Inorg. Chem.* **52**, 9019–9038 (2013).
- 12. Krishnamoorthy, T. et al. Lead-free germanium iodide perovskite materials for photovoltaic applications. *J. Mater. Chem. A.* 3, 23829–23832 (2015).
- 13. Sun, P.-P., Li, Q.-S., Yang, L.-N. & Li, Z.-S. Theoretical insights into a potential lead-free hybrid perovskite: substituting Pb 2+ with Ge 2+. *Nanoscale* 8, 1503–1512 (2016).
- 14. Nagane, S. et al. Lead-free perovskite semiconductors based on germanium-tin solid solutions: structural and optoelectronic properties. J. Phys. Chem. C. 122, 5940–5947 (2018).
- 15. Wang, K., Liang, Z., Wang, X. & Cui, X. Lead replacement in CH3NH3PbI3 perovskites. Adv. Electr. Mater. 1, 1500089 (2015).
- Zhao, P. et al. Device simulation of inverted CH3NH3PbI3- xClx perovskite solar cells based on PCBM electron transport layer and NiO hole transport layer. Sol. Energy 169, 11–18 (2018).
- 17. Conings, B. et al. Intrinsic thermal instability of methylammonium lead trihalide perovskite. Adv. Energy Mater. 5, 1500477 (2015).
- 18. Sun, P.-P., Li, Q.-S., Feng, S. & Li, Z.-S. Mixed Ge/Pb perovskite light absorbers with an ascendant efficiency explored from theoretical view. *Phys. Chem. Chem. Phys.* 18, 14408–14418 (2016).
- 19. Hu, H., Dong, B. & Zhang, W. Low-toxic metal halide perovskites: opportunities and future challenges. *J. Mater. Chem. A.* 5, 11436–11449 (2017).
- Saparov, B. & Mitzi, D. B. Organic-inorganic perovskites: structural versatility for functional materials design. Chem. Rev. 116, 4558–4596 (2016).
- 21. Kim, H.-S. et al. Lead iodide perovskite sensitized all-solid-state submicron thin film mesoscopic solar cell with efficiency exceeding 9%. Sci. Rep. 2, 1–7 (2012).
- Ahmed, A., Riaz, K., Mehmood, H., Tauqeer, T. & Ahmad, Z. Performance optimization of CH3NH3Pb (I1-xBrx) 3 based perovskite solar cells by comparing different ETL materials through conduction band offset engineering. Opt. Mater. 105, 109897 (2020).
- 23. Makableh, Y. F., Aljaiuossi, G. & Al-Abed, R. Comprehensive design analysis of electron transmission nanostructured layers of heterojunction perovskite solar cells. *Superlattices Microstruct.* **130**, 390–395 (2019).
- 24. Kanoun, A.-A., Kanoun, M. B., Merad, A. E. & Goumri-Said, S. Toward development of high-performance perovskite solar cells based on CH3NH3GeI3 using computational approach. *Sol. Energy* **182**, 237–244 (2019).
- Hossain, M. I., Alharbi, F. H. & Tabet, N. Copper oxide as inorganic hole transport material for lead halide perovskite based solar cells. Sol. Energy 120, 370–380 (2015).
- 26. Subbiah, A. S. et al. Inorganic hole conducting layers for perovskite-based solar cells. J. Phys. Chem. Lett. 5, 1748-1753 (2014).
- 27. Kirchartz, T. High open-circuit voltages in lead-halide perovskite solar cells: experiment, theory and open questions. *Phil. Trans. R. Soc. A* 377, 20180286 (2019).
- 28. Belayachi, W. et al. Study of hybrid organic-inorganic halide perovskite solar cells based on MAI [(PbI2) 1-x (CuI) x] absorber layers and their long-term stability. *J. Mater. Sci.: Mater. Electron.* 32, 20684–20697 (2021).
- 29. Wang, P. et al. Cobalt Chloride Hexahydrate Assisted in Reducing Energy Loss in Perovskite Solar Cells with Record Open-Circuit Voltage of 1.20 V. ACS Energy Lett. 6, 2121–2128 (2021).
- 30. Elseman, A. M., Shalan, A. E., Rashad, M. M. & Hassan, A. M. Experimental and simulation study for impact of different halides on the performance of planar perovskite solar cells. *Mater. Sci. Semicond. Process.* 66, 176–185 (2017).
- 31. Bajorowicz, B. et al. Integrated experimental and theoretical approach for efficient design and synthesis of gold-based double halide perovskites. *J. Phys. Chem. C.* **124**, 26769–26779 (2020).
- Haider, S. Z., Anwar, H., Manzoor, S., Ismail, A. G. & Wang, M. A theoretical study for high-performance inverted pin architecture perovskite solar cells with cuprous iodide as hole transport material. *Curr. Appl. Phys.* 20, 1080–1089 (2020).
- 33. Burgelman, M., Nollet, P. & Degrave, S. Modelling polycrystalline semiconductor solar cells. Thin Solid Films 361, 527-532 (2000).
- 34. van Reenen, S., Kemerink, M. & Snaith, H. J. Modeling anomalous hysteresis in perovskite solar cells. J. Phys. Chem. Lett. 6, 3808–3814 (2015).
- 35. Ravishankar, S. et al. Surface polarization model for the dynamic hysteresis of perovskite solar cells. *J. Phys. Chem. Lett.* **8**, 915–921 (2017).
- 36. Courtier, N. E., Richardson, G. & Foster, J. M. A fast and robust numerical scheme for solving models of charge carrier transport and ion vacancy motion in perovskite solar cells. *Appl. Math. Model.* 63, 329–348 (2018).
- 37. Ragb, O., Mohamed, M., Matbuly, M. S. & Civalek, O. An accurate numerical approach for studying perovskite solar cells. *Int. J. Energy Res.* 45, 16456–16477. https://doi.org/10.1002/er.6892 (2021).
- 38. O. Ragb, M. Mohamed, M.S. Matbuly, O. Civalek, Sinc and discrete singular convolution for analysis of three-layer composite of perovskite solar cell, International Journal of Energy Research. (n.d.).
- Shu, C., Yao, Q. & Yeo, K. S. Block-marching in time with DQ discretization: an efficient method for time-dependent problems. Comput. Methods Appl. Mech. Eng. 191, 4587–4597 (2002).
- 40. Ragl, O., Mohamed, M. & Matbuly, M. S. Vibration analysis of magneto-electro-thermo NanoBeam resting on nonlinear elastic foundation using sinc and discrete singular convolution differential quadrature method. *Mod. Appl. Sci.* 13, 49 (2019).
- 41. Ragb, O., Mohamed, M. & Matbuly, M. S. Free vibration of a piezoelectric nanobeam resting on nonlinear Winkler-Pasternak foundation by quadrature methods. *Heliyon*. 5, e01856. https://doi.org/10.1016/j.heliyon.2019.e01856 (2019).
- 42. Azri, F., Meftah, A., Sengouga, N. & Meftah, A. Electron and hole transport layers optimization by numerical simulation of a perovskite solar cell. Sol. Energy 181, 372–378 (2019).
- 43. Î. Alam, M.A. Ashraf, Effect of different device parameters on tin-based perovskite solar cell coupled with In2S3 electron transport layer and CuSCN and Spiro-OMeTAD alternative hole transport layers for high-efficiency performance, Energy Sources, Part A: Recovery, Utilization, and Environmental Effects. 1–17. (2020)
- 44. Calado, P. et al. Evidence for ion migration in hybrid perovskite solar cells with minimal hysteresis. Nat. Commun. 7, 1–10 (2016).
- 45. Zandi, S. & Razaghi, M. Finite element simulation of perovskite solar cell: A study on efficiency improvement based on structural and material modification. Sol. Energy 179, 298–306 (2019).

- 46. Wang, S. et al. Effective lifetime of non-equilibrium carriers in semiconductors from non-adiabatic molecular dynamics simulations. *Nat. Comput. Sci.* **2**, 486–493 (2022).
- Yuan, Y. et al. Shallow defects and variable photoluminescence decay times up to 280 μs in triple-cation perovskites. Nat. Mater. 23, 391–397 (2024).
- 48. Reichert, S. et al. Probing the ionic defect landscape in halide perovskite solar cells. Nat. Commun. 11, 6098 (2020).
- 49. J.A. Nelson, The physics of solar cells, World Scientific Publishing Company, (2003).
- 50. Foster, J. M., Kirkpatrick, J. & Richardson, G. Asymptotic and numerical prediction of current-voltage curves for an organic bilayer solar cell under varying illumination and comparison to the Shockley equivalent circuit. *J. Appl. Phys.* **114**, 104501 (2013).
- 51. Civalek, Ö. Free vibration of carbon nanotubes reinforced (CNTR) and functionally graded shells and plates based on FSDT via discrete singular convolution method. *Compos. B Eng.* 111, 45–59 (2017).
- 52. Civalek, Ö. & Kiracioglu, O. Free vibration analysis of Timoshenko beams by DSC method. *Int. J. Numerical Methods Biomed. Eng.* 26, 1890–1898 (2010).
- 53. Wan, D. C., Zhou, Y. C. & Wei, G. W. Numerical solution of incompressible flows by discrete singular convolution. *Int. J. Numer. Meth. Fluids* 38, 789–810 (2002).
- 54. Zhang, L., Xiang, Y. & Wei, G. W. Local adaptive differential quadrature for free vibration analysis of cylindrical shells with various boundary conditions. *Int. J. Mech. Sci.* 48, 1126–1138 (2006).
- 55. Shu, C. & Richards, B. E. Application of generalized differential quadrature to solve two-dimensional incompressible Navier-Stokes equations. *Int. J. Numer. Meth. Fluids* 15, 791–798 (1992).
- 56. Caputo, M. Linear models of dissipation whose Q is almost frequency independent—II. Geophys. J. Int. 13, 529-539 (1967).
- 57. M. Weilbeer, Efficient numerical methods for fractional differential equations and their analytical background, (2006).
- 58. Su, P. et al. Enhanced photovoltaic properties of perovskite solar cells by TiO2 homogeneous hybrid structure. *Royal Soc. Open Sci.* **4**, 170942 (2017).
- 59. Rai, N., Rai, S., Singh, P. K., Lohia, P. & Dwivedi, D. K. Analysis of various ETL materials for an efficient perovskite solar cell by numerical simulation. *J. Mater. Sci.: Mater. Electron.* 31, 16269–16280 (2020).
- 60. Jeong, M. J. et al. Boosting radiation of stacked halide layer for perovskite solar cells with efficiency over 25%. *Joule* 7, 112–127 (2023).
- Srivastava, M., Surana, K., Singh, S., Singh, P. K. & Singh, R. C. Highly efficient sandwich structured Perovskite solar cell using PEDOT: PSS in room ambient conditions, Materials Today. *Proceedings* 34, 675–678 (2021).
- 62. Courtier, N. E., Cave, J. M., Foster, J. M., Walker, A. B. & Richardson, G. How transport layer properties affect perovskite solar cell performance: insights from a coupled charge transport/ion migration model. *Energy Environ. Sci.* 12, 396–409 (2019).

Author contributions

Conceptualization, E.M.A, M.M., O.R., and M.S.; methodology, E.M.A, M.M., O.R., and M.S.; software, M.M.; validation, M.M. and E.M.A; formal analysis, investigation, O.R., M.S., and M.M.; resources, E.M.A; data curation, writing—original draft preparation, O.R., M.S., and M.M.; writing—review and editing, M.M, E.M.A; visualization, supervision, E.M.A, O.R. and M.S; Funding, E.M.A. All authors have read and agreed to the published version of the manuscript.

Funding

This work was supported and funded by the Deanship of Scientific Research at Imam Mohammad Ibn Saud Islamic University (IMSIU) (grant number IMSIU-DDRSP2503).

Declarations

Competing interests

The authors declare no competing interests.

Additional information

Correspondence and requests for materials should be addressed to E.M.A. or M.M.

Reprints and permissions information is available at www.nature.com/reprints.

Publisher's note Springer Nature remains neutral with regard to jurisdictional claims in published maps and institutional affiliations.

Open Access This article is licensed under a Creative Commons Attribution-NonCommercial-NoDerivatives 4.0 International License, which permits any non-commercial use, sharing, distribution and reproduction in any medium or format, as long as you give appropriate credit to the original author(s) and the source, provide a link to the Creative Commons licence, and indicate if you modified the licensed material. You do not have permission under this licence to share adapted material derived from this article or parts of it. The images or other third party material in this article are included in the article's Creative Commons licence, unless indicated otherwise in a credit line to the material. If material is not included in the article's Creative Commons licence and your intended use is not permitted by statutory regulation or exceeds the permitted use, you will need to obtain permission directly from the copyright holder. To view a copy of this licence, visit https://creativecommons.org/licenses/by-nc-nd/4.0/.

© The Author(s) 2025